Borehole heat flow along the eastern flank of the Juan de Fuca Ridge, including effects of anisotropy and temperature dependence of sediment thermal conductivity
- Appendix -

Dan F.C. Pribnow
Joint Geoscientific Research Institute, GGA
Stilleweg 2
D-30655 Hannover, Germany

Earl E. Davis
Pacific Geoscience Centre, PGC
Geological Survey of Canada
P.O. Box 6000
Sidney, B.C. V8L 4B2
Canada

Andrew T. Fisher
Earth Sciences Department and Institute of Tectonics
University of Santa Cruz, California
Santa Cruz, CA 95064
USA

Appendix

A1. Introduction

This Appendix contains detailed descriptions of experimental and analytical methods used in this study. The divided bar method to determine thermal conductivity is described, emphasising aspects of anisotropy in comparison to the needle probe approach and effects of temperature. The influence of porosity and sea water properties on anisotropy and temperature effects is discussed. Various methods for the calculation of thermal resistance are presented and evaluated. Finally, the consequences for the heat flow calculation are analyzed.

A2. Divided-Bar Thermal Conductivity Measurements

A2.1 The Divided-Bar Method

There are two major differences between divided-bar and ship-board line-source thermal conductivity methods: (1) the line-source method is transient while the divided-bar is steady-state; (2) divided-bar measurements provide one-dimensional data (Fig. A1), whereas the line-source method produces a scalar value from a plane (Fig. A2). The ability to measure thermal conductivity in a single direction makes the divided-bar method suitable for the determination of anisotropy (e.g., Pribnow and Sass, 1995).

The divided-bar is a comparative method in which the temperature drop across a disk of rock or a cylindrical cell containing water-saturated material is compared with that across a disk of reference material of known thermal conductivity (Fig. A1; see also Sass et al., 1992; Pribnow and Sass, 1995). It is in theory and by design a one-dimensional method to determine thermal conductivity parallel to the divided-bar axis. Samples are prepared with their cylindrical axis parallel to the desired direction of conductivity to be determined. The

commercial instrument COM-800 (*Holometrix Inc.*) was used at the Joint Geoscientific Research Institute GGA in Hannover, Germany, for this study.

A technique for subsampling soft sediments was adapted to prepare disks of unconsolidated material. These subsamples were taken along horizontal and vertical orientations, expected to coincide with the two principle components of thermal conductivity. Figure A3 shows the sampling procedure for a sample representative of the vertical thermal conductivity component in a divided-bar measurement.

The walls of the filled cell are made of plexiglas with a low thermal conductivity to prevent horizontal heat loss during the measurement. The copper lids are thermally "invisible" in the divided-bar stack due to a thermal conductivity of about 400 $Wm^{-1}K^{-1}$. Similar disks are used to measure the thermal conductivity of cuttings (small rock fragments) from drilling hard rocks (Sass et al., 1971). The results of these measurements are corrected for the influence of the cell itself by considering the outer and inner diameter of the cell wall (OD = 50 mm and ID = 46 mm, respectively), the cell wall conductivity ($\lambda_{CELL} = 0.1$ $Wm^{-1}K^{-1}$), the desired thermal conductivity of the sample (λ_{SMPL}) and the measured value (λ_{MEAS}) of the filled cell (Sass et al., 1971):

$$\lambda_{SMPL} = \frac{OD^2}{ID^2} \cdot \lambda_{MEAS} - \frac{OD^2 - ID^2}{ID^2} \cdot \lambda_{CELL} = 1.181 \cdot \lambda_{MEAS} - 0.029 \qquad \text{(A1)}$$

A total of 15 whole-round samples were tested, two from Hole 1026A and 13 from Hole 1027B. Three cores contained sand, the rest were mud. The depths of samples range from 17 mbsf to 440 mbsf (Tab. A1). For each sample, an attempt was made to first subsample a vertical disk and then, in a second step, subsample a horizontal disk (Fig. A3). The latter failed in four cases; in one case, both attempts failed.

Thermal conductivity is determined continuously at a rate of about one value per minute while the sample is adjusted to a set of defined temperature points. A measurement for a specific temperature point is accepted if (1) the desired mean sample temperature is reached and constant within ± 1 °C, and (2) the results of the last 8 measurements (about 8 minutes) are reproduced within 1 %. Therefore, ambient temperatures for different subsamples (horizontal and vertical) may be close but are not identical (T_{meas} in Tab. A1). Figure A4 shows good agreement between divided-bar results and shipboard line-source measurements, both at laboratory temperature. For divided-bar measurements, the vertical conductivity is always lower than the horizontal.

Of the 25 disk samples tested by the divided-bar, three results were rejected due to obvious drying of the material during measurement. Usually, the sealing of the copper lids on the cell ring (Fig. A3, step 5) was sufficient to prevent water loss of the sample during the 6 to 18 hour-long experiment with temperatures up to 60 °C. To identify water loss, disks were weighed before and after the experiment (typical values: total cell weight of 150 g with a sediment content of 40 g). If a total weight loss of more than 0.1 % was observed - usually together with a strong decrease of thermal conductivity with increasing duration and temperature - the thermal conductivity results were rejected.

A2.2 Thermal Conductivity Anisotropy

Thermal conductivity is defined by three principal components λ_A, λ_B, and λ_C along the axes A, B, and C, respectively. Due to layering, many rocks are transversally isotropic ($\lambda_A = \lambda_B$). The thermal conductivity tensor can then be defined by two principal components that are perpendicular ($\lambda_{PER} = \lambda_C$) and parallel ($\lambda_{PAR} = \lambda_A = \lambda_B$) to the layering. Given a general horizontal layering for Leg 168 sediments, thermal conduction is expected to be greater in the horizontal direction than vertically. For this case, the core-parallel component is horizontal

(λ_{HOR}=λ_{PAR}) and the perpendicular component is vertical (λ_{VER}=λ_{PER}). In this study, we define the thermal conductivity anisotropy K as (e.g., Popov et al., 1999):

$$K = \frac{\lambda_{HOR}}{\lambda_{VER}} = \frac{\lambda_{PAR}}{\lambda_{PER}} \tag{A2}$$

For heat flow calculations, the vertical component of thermal conductivity, which is parallel to the direction of the measured temperature gradient, was calculated using line-source values and the assumed anisotropy. The line-source provides a two-dimensional value of thermal conductivity (λ_{LS}) for a plane perpendicular to the needle axis (Fig. A2). The result obtained from a measurement of an anisotropic sample is related to the orientations of the principal axes of the thermal conductivity tensor (λ_A, λ_B, λ_C):

$$\lambda_{LS} = \sqrt{\lambda_A \cdot \lambda_B \cdot \cos^2(\gamma) + \lambda_A \cdot \lambda_C \cdot \cos^2(\beta) + \lambda_B \cdot \lambda_C \cdot \cos^2(\alpha)} \tag{A3}$$

where α, β, and γ are angles between the line-source axis and principal axes of thermal conductivity A, B, and C, respectively (Popov et al., 1999). Considering the horizontal position of the line-source for routine measurements performed during Leg 168 (Fig. A2) and the horizontal anisotropy of Leg 168 sediments, $\alpha = 0°$ and $\beta = \gamma = 90°$, equation (A3) can be simplified to

$$\lambda_{LS} = \sqrt{\lambda_{HOR} \cdot \lambda_{VER}} \tag{A4}$$

Therefore, in case the needle probe is positioned parallel to the bedding, the measured thermal conductivity is the geometric mean of the parallel and perpendicular components. The desired vertical component of thermal conductivity is calculated as:

$$\lambda_{VER}(z) = \frac{\lambda_{LS}(z)}{\sqrt{K(z)}} \tag{A5}$$

A2.3 Temperature Dependence of Thermal Conductivity

For 12 of the 22 samples with acceptable results from divided-bar measurements (horizontal and vertical), thermal conductivity was measured within a temperature range between 5 °C and 60 °C, and for 10 of these, at 20 °C and at the corresponding *in-situ* temperature (Tab. A1 and Fig. 5). The effect of temperature is related to the thermal conductivity at laboratory (room) temperature, $\lambda_{rt} = \lambda(20\ °C)$: if λ_{rt} is low, conductivity increases with temperature; if λ_{rt} is intermediate, conductivity does not change with temperature; if λ_{rt} is high, conductivity decreases with temperature. Figure A5 shows a linear temperature dependence of thermal conductivity ($\Delta\lambda/\Delta T$) as a function of λ_{rt}. The linear regression of this dataset provides a means to calculate a value of thermal conductivity for any temperature based only on λ_{rt}:

$$\begin{aligned} \lambda(T) &= \lambda_{rt} + \Delta\lambda/\Delta T \cdot (T - 20) \\ &= \lambda_{rt} + (5.4 \cdot 10^{-3} - 4.7 \cdot 10^{-3} \cdot \lambda_{rt}) \cdot (T - 20) \end{aligned} \tag{A6}$$

Thus, the correction can be applied directly to shipboard laboratory values by substituting λ_{LS} for λ_{rt} in equation (A6). The depth of a sample is translated into an *in-situ* temperature with the average temperature gradient of the corresponding hole (Fig. 2).

A2.4 The Influence of Porosity

In this brief discussion, anisotropy and temperature corrections are generalized for cases where only porosity and line-source thermal conductivity values are available. The amount of

porewater in the sample has influence on both anisotropy and temperature effects. Water is isotropic and decreases the bulk anisotropy with increasing porosity for a sample with anisotropic matrix. The temperature dependence of water is different from that of the matrix. To separate these effects, the geometric mixing model is used:

$$\lambda_{BLK} = \lambda_{FLD}^{\phi} \cdot \lambda_{MAT}^{1-\phi} \tag{A7}$$

where ϕ is porosity, and the subscripts BLK, FLD and MAT stand for bulk, fluid, and matrix, respectively. It is noteworthy that the geometric mean is a simple and robust mixing model that is widely used, but not physically based (Woodside and Messmer, 1961; Sass et al., 1971; Pribnow and Umsonst, 1993; Pribnow and Sass, 1995). Sample porosities for this study were measured during Leg 168 (Davis et al., 1997a) and are listed in Table A1.

A2.4.1 Anisotropy. Based on the geometric mean model (eq. A7), the matrix anisotropy can be estimated by:

$$K_{BLK} = \frac{\lambda_{FLD}^{\phi} \cdot \lambda_{MAT,h}^{1-\phi}}{\lambda_{FLD}^{\phi} \cdot \lambda_{MAT,v}^{1-\phi}} = K_{MAT}^{1-\phi}, \tag{A8}$$

where K is anisotropy (eq. A2), and subscripts v and h represent vertical and horizontal components, respectively. For this study, the average of the matrix anisotropy calculated with equation (A8) is $K_{MAT} = 1.4 \pm 0.2$. Davis and Seemann (1994) suggest a mean matrix conductivity of 3.3 $Wm^{-1}K^{-1}$ for the horizontal and 2.6 $Wm^{-1}K^{-1}$ for the vertical component, indicating similar matrix anisotropy of $K_{MAT} = 1.3$. With equations (A6) to (A8) and an assumed matrix conductivity, the bulk vertical conductivity can be calculated from shipboard line-source measurements (λ_{LS}) and sample porosity (ϕ) with:

$$\lambda_{VER}(z) = \frac{\lambda_{LS}(z)}{\sqrt{(K_{MAT})^{1-\phi}}} \tag{A9}$$

A2.4.2 Temperature Dependence. The temperature dependence between 0 °C and 60 °C of sea water, $\lambda_{FLD}(T)$, and matrix, $\lambda_{MAT}(T)$, can be represented by (see Tab. A2):

$$\lambda_{FLD}(T) = 0.56 + 1.44 \cdot 10^{-3} \cdot T \tag{A10 a}$$

$$\lambda_{MAT}(T) = 2.93 - 5.11 \cdot 10^{-3} \cdot T \tag{A10 b}$$

with T in °C. Based on the geometric mixing model, the general temperature dependence of the bulk conductivity can be expressed by:

$$\lambda_{BLK}(T) = \lambda_{FLD}^{\phi}(T) \cdot \lambda_{MAT}^{1-\phi}(T) \tag{A11}$$

This approach is supported by the good agreement between measured and calculated (eq. A11) temperature dependence (Fig. 5).

An analysis similar to that used for bulk conductivity yields a linear temperature dependence of matrix thermal conductivity as a function of conductivity at laboratory temperature (Fig. A6). Whereas the bulk conductivity shows both positive and negative temperature coefficients depending on sediment porosity, matrix conductivity generally decreases with increasing temperature, particularly at high λ_{rt} values. Adapting equation (A11) for λ_{rt} and considering that $\lambda_{FLD}(20\ °C) = 0.6\ Wm^{-1}K^{-1}$, an equation describing the temperature dependence of matrix thermal conductivity for Leg 168 sediments based on sample porosity and laboratory temperature values is similar to equation (A6):

$$\lambda_{MAT}(T)=\left(\frac{\lambda_{rt}}{(0.6)^{\phi}}\right)^{\frac{1}{1-\phi}}+\left(8.0\cdot10^{-3}-5.4\cdot10^{-3}\cdot\left(\frac{\lambda_{rt}}{(0.6)^{\phi}}\right)^{\frac{1}{1-\phi}}\right)\cdot(T-20) \qquad \text{(A12)}$$

When combined with equation (A10a and A11), this allows estimation of *in-situ* bulk thermal conductivity from λ_{rt}, porosity, and temperature data alone.

A3 Thermal Resistance

Based on the experimental thermal conductivity anisotropy and temperature dependence, we calculated vertical thermal resistance values (Ω) along the Leg 168 transect. Depths and thicknesses of sediment layers are generally well known from shipboard observations, although core recovery was poor in sandy intervals (Davis et al., 1997a). One standard approach is to assume that each conductivity value λ_k, at depth $z_{\lambda,k}$, is representative of a layer between $z_{\lambda,k}$ and $z_{\lambda,k-1}$, the next shallowest measurement:

$$\Omega=\sum\frac{z_{\lambda,k}-z_{\lambda,k-1}}{\lambda_k} \qquad \text{(A13)}$$

This approach is inappropriate in this case because sandy intervals are often skipped between widely spaced measurements. Instead, we estimate the thermal resistance based on average thermal conductivity values for sand and mud, λ_S and λ_M, and then we use core descriptions to assign sand and mud layers.

The thermal resistance is calculated for the interval between two temperature measurements T_{j-1} and T_j, at depths $z_{T,j-1}$ and $z_{T,j}$, with the harmonic mean and weighted by the total thickness $d_{S,j}$ and $d_{M,j}$ of sand and mud layers within this depth interval:

$$\Omega(z_{T,j})=\Omega(z_{T,j-1})+\frac{1}{z_{T,j}-z_{T,j-1}}\cdot\left(\frac{d_{S,j}}{\lambda_S}+\frac{d_{M,j}}{\lambda_M}\right) \qquad \text{(A14)}$$

This shipboard approach (Davis et al., 1997a) neglects any depth dependence on porosity and thermal conductivity. We now account for the porosity decrease with depth by: (1) calculating the thermal resistance of mud ($\Omega_{M,j}$) with equation (A13) for the interval between two temperature measurements T_{j-1} and T_j ($z_{T,j}$ - $z_{T,j-1}$), based on individual measurements in mud ($\lambda_{M,k}$); (2) calculating the thermal resistance of sand layers ($\Omega_{S,j}$) in the same depth interval with equation (A14), based on an average value for sand ($\lambda_{S,j}$) because the measurements do not indicate a systematic change with depth; and (3) combining the two resistance values, weighted with the total thickness $d_{S,j}$ and $d_{M,j}$ of sand and mud layers (as determined by shipboard core descriptions), in relation to the depth interval $z_{T,j}$ - $z_{T,j-1}$:

$$\begin{aligned}\Omega(z_{T,j})&=\Omega(z_{T,j-1})+\frac{1}{z_{T,j}-z_{T,j-1}}\cdot\left(d_{S,j}\cdot\Omega_{S,j}+d_{M,j}\cdot\Omega_{M,j}\right)\\&=\Omega(z_{T,j-1})+\frac{1}{z_{T,j}-z_{T,j-1}}\cdot\left(d_{S,j}\cdot\frac{d_{S,j}}{\lambda_{S,j}}+d_{M,j}\cdot\sum\frac{z_{M,k}-z_{M,k-1}}{\lambda_{M,k}}\right)\end{aligned} \qquad \text{(A15)}$$

In this way, both systematic changes in mud conductivity and the occurance of sand layers are included in the analysis. Figure A7 shows an example for the calculation of thermal resistance with equation (A15) for a layer between two temperature measurements in Hole 1023A.

A4 Heat Flow Calculations

To evaluate the significance of this method for thermal resistance calculation plus the consideration of anisotropy and temperature effects on conductivity, the recalculation of heat flow is performed in several steps. $\mathbf{q_{IR}}$ is shipboard heat flow (Davis et al., 1997a), using one average thermal conductivity for mud and one for sand (eq. A14), ignoring variations in conductivity with depth but considering each layer. $\mathbf{q_{STP}}$ is heat flow calculated from a thermal resistance that is based on all conductivity values (eq. A13), considering variations with depth but neglecting layers not represented by measurements. $\mathbf{q_{M,S}}$ is heat flow based on a combination of using the q_{IR} method for sand layers and the q_{STP} method for mud layers (eq. A15), thus considering variations with depth for mud and each sand layer. $\mathbf{q_v}$ is the $q_{M,S}$ method based on vertical conductivity corrected for mud anisotropy (A5); $\mathbf{q_{v,T}}$ is the $q_{M,S}$ method based on vertical conductivity corrected for anisotropy (A5) and temperature (eq. A6); for the mean sand conductivity of a layer ($\lambda_{S,j}$), the average conductivity at laboratory temperature for sand (1.53 $Wm^{-1}K^{-1}$) is corrected for the *in-situ* temperature (eq. A6), which is relevant in the considered depth interval.

Table A3 lists all previous and revised heat flow values. The relative differences are discussed in relation to the used methods. $\mathbf{q_{STP}}$ **vs** $\mathbf{q_{IR}}$: Consideration of the observed thermal conductivity decrease close to seafloor (Fig. 3) by using the q_{STP} method results in heat flow values that are 2 % to 14 % lower than those based on constant mud conductivity (q_{IR}). The largest change occurs for Hole 1026A (-14 %), where 30 % of the drilled section comprises sand (Davis et al., 1997a). These layers with higher conductivity are considered fully in the q_{IR} method but neglected in the q_{STP} method, unless the number of conductivity measurements from sand layers is representative. $\mathbf{q_{M,S}}$ **vs** $\mathbf{q_{STP}}$: Consideration of all sand layers ($q_{M,S}$) has no effect on measurements in a pure mud environment (1031A, 1032A) but increases heat flow by up to 43 % (Hole 1026A), where sand layers occur. $\mathbf{q_v}$ **vs** $\mathbf{q_{M,S}}$: Due to anisotropy, the vertical conductivity reduces heat flow values by 5 % to 9 %. $\mathbf{q_{v,T}}$ **vs** $\mathbf{q_v}$: Correcting vertical conductivity for temperature causes a negligible (less than 1 %) decrease of heat flow. $\mathbf{q_{v,T}}$ **vs** $\mathbf{q_{IR}}$: After improving resistivity calculations and correcting for anisotropy and temperature ($q_{v,T}$), heat flow is reduced by up to 12 % for all sites except 1026A, where $q_{v,T}$ is 16 % higher. The general reduction of heat flow results from lower vertical conductivity in this study, although at Hole 1026A, this effect is overwhelmed by inclusion of thick sand layers. The impact of the temperature correction is generally small because thermal conductivity values at laboratory temperature are close to 1.2 $Wm^{-1}K^{-1}$ (Fig. A3).

Consequences of these additional aspects for Leg 168 borehole heat flow are: (1) a 2 % to 14 % decrease resulting from consideration of low conductivities of high-porous sediments close to seafloor (upper 5 mbsf); (2) an increase up to 20 % by considering all known sand layers with higher conductivity; (3) a 5 % to 9 % decrease resulting from the use of vertical conductivity; and (4) a decrease less than 1% based on temperature corrections.

Appendix References

Davis, E.E., and D.A. Seemann, Anisotropic thermal conductivity of pleistocene turbidite sediments of the northern Juan de Fuca Ridge, *Proceedings of the Ocean Drilling Program, Scientific Results*, Vol. *139*, 559 - 564, 1994.

Davis, E.E., A.T. Fisher, J.V. Firth et al., *Proceedings of the Ocean Drilling Program, Initial Results*, Vol. *168*, pp. 470, 1997a.

Davis, E.E., D.S. Chapman, H. Villinger, S. Robinson, J. Grigel, A Rosenberger, and D.F.C. Pribnow, Seafloor heat flow on the eastern flank of the Juan de Fuca Ridge: data from "FlankFlux" studies through 1995, *Proceedings of the Ocean Drilling Program, Initial Results*, Vol. *168*, 23 - 33, 1997b.

Davis, E.E., D.S. Chapman, K. Wang, H. Villinger, A.T. Fisher, S.W. Robinson, J. Grigel, D.F.C. Pribnow, J. Stein, and K. Becker, Regional heat-flow variations across the sedimented Juan de Fuca Ridge and lateral hydrothermal heat transport, *J. Geophys. Res.*, *104*, 17675-17688, 1999.

Defant, A., *Physical Oceanography*, Vol. 1, Pergamon, New York, NY, 1961.

Keenan, J.H., F.G. Keyes, P.G. Hill, and J.G Moore, *Steam Tables: Thermodynamic Properties of Water, Including Vapor, Liquid, and Solid Phases*, Wiley, New York, NY, 1978.

Popov Y.A, D.F.C. Pribnow, J.H. Sass, C.F. Williams, and H. Burkhardt, Characterization of rock thermal conductivity by high-resolution optical scanning, *Geothermics, in press*, 1999.

Pribnow, D.F.C., and J.H. Sass, Determination of thermal conductivity for deep boreholes, *J. Geophys. Res.*, *100*, 9981 - 9994, 1995.

Pribnow, D.F.C., and T. Umsonst, Estimation of thermal conductivity from the mineral composition: influence of fabric and anisotropy, *Geophys. Res. Let., 20,* 2199-2202, 1993.

Sass, J.H., A.H. Lachenbruch, and R. Munroe, Thermal conductivity of rocks from measurements on fragments and its application to heat flow determinations, *J. Geophys. Res.*, *76*, 3391 - 3401, 1971.

Sass, J.H., A.H. Lachenbruch, T. Moses, and P. Morgan, Heat flow from a scientific research well at Cajon Pass, California, *J. Geophys. Res.*, *97*, 5017 - 5030, 1992.

Woodside, W., and J. Messmer, Thermal conductivity of porous media, *J. Appl. Phys., 32,* 1688-1706, 1961.

Zoth, G., and R. Hänel, Appendix, in: R. Hänel, L. Rybach and I. Stegena (eds), *Handbook of Terrestrial Heat-Flow Density Determination,* Kluwer Academic Publishers, Dordrecht, pp. 449-466, 1988.

Appendix Tables

Table A1. Results of Divided-Bar Measurements

Core	Litho-logy	Depth (mbsf)	Poro-sity (%) [1]	In-situ temp. (ºC) [2]	T_{meas} of λ_{HOR} (ºC) [3, 4]	λ_{HOR} ($Wm^{-1}K^{-1}$) [4]	T_{meas} of λ_{VER} (ºC) [3, 5]	λ_{VER} ($Wm^{-1}K^{-1}$) [5]	Aniso-tropy
168-1026A-									
4H-3, 40-55	sand	28.0	35.8	8.6	-	-	5.2	1.57	-
					-	-	8.0	1.55	-
					-	-	10.0	1.55	-
					-	-	15.3	1.54	-
					-	-	19.8	1.51	-
					-	-	30.3	1.47	-
					-	-	39.8	1.40	-
					-	-	50.3	1.35	-
					-	-	60.2	1.35	-
11H-2,80-95	sand	93.3	37.0	24.4	4.8	1.76	4.9	1.74	1.02
168-1027B-									
3H-3, 55-70	mud	17.1	64 *	3.6	5.4	1.19	4.9	1.01	1.18
					8.4	1.19	7.9	1.03	1.16
					9.4	1.20	9.9	1.02	1.17
					15.3	1.20	14.8	1.01	1.19
					20.3	1.20	19.8	1.01	1.18
					30.3	1.18	29.8	1.02	1.15
					40.4	1.18	39.8	0.99	1.19
					50.2	1.21	49.8	0.99	1.22
					60.1	1.23	59.7	1.04	1.18
6H-6, 70-85	mud	50.4	53.8	7.0	7.3	1.28	6.8	1.04	1.24
					20.1	1.29	19.6	1.04	1.24
7H-1, 55-70	sand	52.2	37.4	7.2	-	-	4.8	1.75	-
					-	-	7.3	1.75	-
					-	-	10.7	1.75	-
					-	-	15.7	1.72	-
					-	-	20.7	1.71	-
					-	-	29.6	1.69	-
					-	-	39.6	1.67	-
					-	-	49.6	1.69	-
					-	-	59.5	1.66	-
8H-1, 25-40	mud	61.3	56 *	8.2	5.4	1.25	-	-	-
					7.4	1.26	-	-	-
					10.9	1.26	-	-	-
					15.3	1.25	14.8	1.10	1.14
					19.8	1.25	20.6	1.10	1.13
					30.3	1.25	30.6	1.09	1.14
					40.3	1.23	40.6	1.11	1.11
					50.2	1.25	50.1	1.10	1.14
					60.2	1.24	60.6	1.09	1.14
17X-3, 20-35	mud	148.7	56.5	17.2	14.6	1.34	-	-	-
					16.6	1.34	-	-	-
					19.6	1.33	-	-	-
22X-3, 90-105	mud	197.4	56.6	22.2	5.8	0.90	-	-	-
					7.8	0.88	-	-	-
					9.8	0.89	-	-	-
					15.7	0.91	-	-	-
					20.8	0.91	-	-	-
					29.7	0.94	-	-	-
					39.7	0.95	-	-	-
					50.7	0.98	-	-	-
					60.7	0.99	-	-	-

Core	Litho-logy	Depth (mbsf)	Poro-sity (%) [1]	In-situ temp. (ºC) [2]	T_{meas} of λ_{HOR} (ºC) [3, 4]	λ_{HOR} ($Wm^{-1}K^{-1}$) [4]	T_{meas} of λ_{VER} (ºC) [3, 5]	λ_{VER} ($Wm^{-1}K^{-1}$) [5]	Aniso-tropy
29X-1, 98-113	mud	261.9	52.4	28.8	24.6	1.20	24.6	0.98	1.22
					29.3	1.20	28.8	0.98	1.22
					34.9	1.21	34.6	0.98	1.24
32X-3, 110-125	mud	293.9	57.4	32.1	-	-	5.0	0.88	-
					-	-	7.6	0.91	-
					-	-	10.6	0.91	-
					-	-	15.7	0.91	-
					-	-	19.7	0.91	-
					-	-	30.0	0.92	-
					-	-	39.7	0.93	-
					-	-	49.9	0.95	-
					-	-	60.1	0.97	-
35X-2, 85-100	mud	321.1		34.9	-	-	5.0	0.93	-
					-	-	8.0	0.95	-
					-	-	10.1	0.94	-
					-	-	15.6	0.95	-
					-	-	19.3	0.94	-
					-	-	30.9	0.95	-
					-	-	39.2	0.96	-
					-	-	50.6	0.97	-
					-	-	60.1	0.98	-
38X-5, 80-95	mud	354.5	52.1	38.4	5.5	1.13	5.0	0.99	1.14
					7.6	1.14	7.6	1.01	1.13
					9.6	1.15	10.1	1.01	1.06
					15.1	1.15	14.6	1.01	1.06
					20.7	1.13	19.7	1.01	1.05
					30.4	1.15	29.9	1.01	1.09
					39.7	1.15	40.0	1.01	1.08
					50.9	1.17	49.5	1.03	1.10
					59.4	1.16	60.2	1.04	1.07
41X-2, 15-30	mud	378.3	49.2	40.8	20.1	1.35	20.1	1.00	1.35
					41.1	1.36	40.6	1.02	1.34
44X-2, 95-110	mud	407.9	49.4	43.9	4.9	1.26	-	-	-
					7.0	1.29	-	-	-
					10.9	1.28	-	-	-
					14.8	1.29	-	-	-
					19.9	1.28	-	-	-
					29.8	1.29	-	-	-
					39.9	1.30	-	-	-
					49.8	1.29	-	-	-
					59.8	1.29	-	-	-
47X-4, 60-75	mud	439.3	45 *	47.1	-	-	20.0	1.05	-
					-	-	47.0	1.09	-

[1] Porosity values with * are interpolated from neighboring samples.

[2] The *in-situ* temperature of the samples is derived from the known temperature gradients.

[3] T_{meas} indicates the sample temperature during the measurement.

[4] λ_{HOR} is the horizontal thermal conductivity.

[5] λ_{VER} is the vertical thermal conductivity.

Table A2. Thermal Conductivity of Matrix and Water

temperature (°C)	thermal matrix[1]	conductivity ($Wm^{-1}K^{-1}$) fresh water[2]	sea water[3]
0	2.95	0.579	0.556
20	2.82	0.615	0.590
40	2.71	0.644	0.618
60	2.61	0.666	0.639

[1] Acidic rocks; Zoth and Haenel (1988)

[2] Keenan et al. (1978)

[3] 4% less than fresh water; Defant (1961)

Table A3. Calculated Heat Flow for Leg 168 Sites Based on Different Methods and Considering Effects of Anisotropy and Temperature

Hole	q_{IR} (eq. 18) [mW m^{-2}]	q_{STP} (eq. 17) [mW m^{-2}]	$q_{M,S}$ (eq. 19) [mW m^{-2}]	q_v [mW m^{-2}] [1]	$q_{v,T}$ [mW m^{-2}] [2]
1023A	84	76	92	85	84
1024B	146	134	150	137	136
1025B	443	416	485	446	440
1026A	328	281	401	380	379
1026C	345	336	377	346	345
1027B	135	125	142	130	129
1028A	457	446	482	442	439
1029A	341	313	366	336	334
1030B	956	930	956	881	873
1031A	1087	1049	1049	967	958
1032A	299	291	291	266	267

[1] Equation (A5) plus anisotropy correction of conductivity

[2] Equation (A5) plus anisotropy and temperature correction of conductivity

Appendix Figures

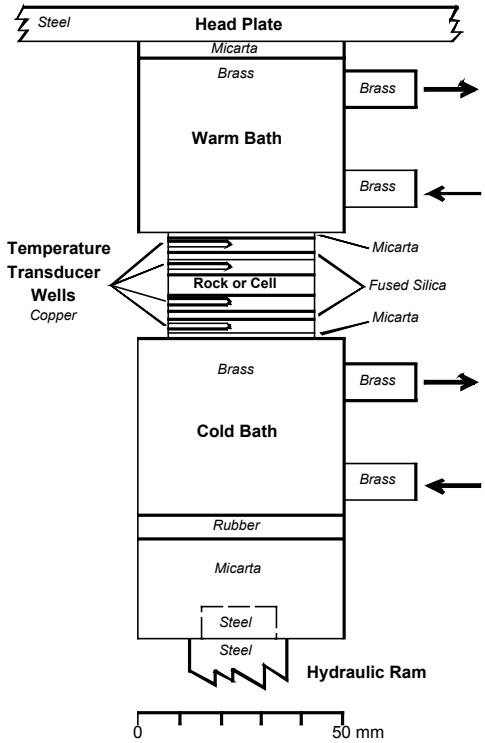

Figure A1. Divided bar method to measure thermal conductivity. The result of such a measurement can clearly be assigned to the direction parallel to the stack axis (after: Pribnow & Sass, 1995).

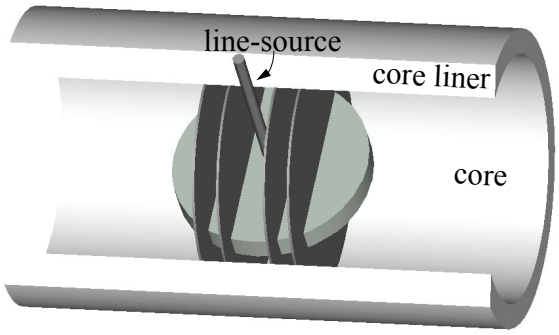

Figure A2. Scheme of thermal conductivity measurements with a shipboard line-source. For clarity, the core is not shown and the core liner is cut open. The thin, dark planes represent horizontal bedding in the sediment core. The thick, light-gray disk indicates the plane from which the line-source scans the thermal conductivity. The result of such a measurement is a scalar value composed of horizontal and vertical thermal conductivity components.

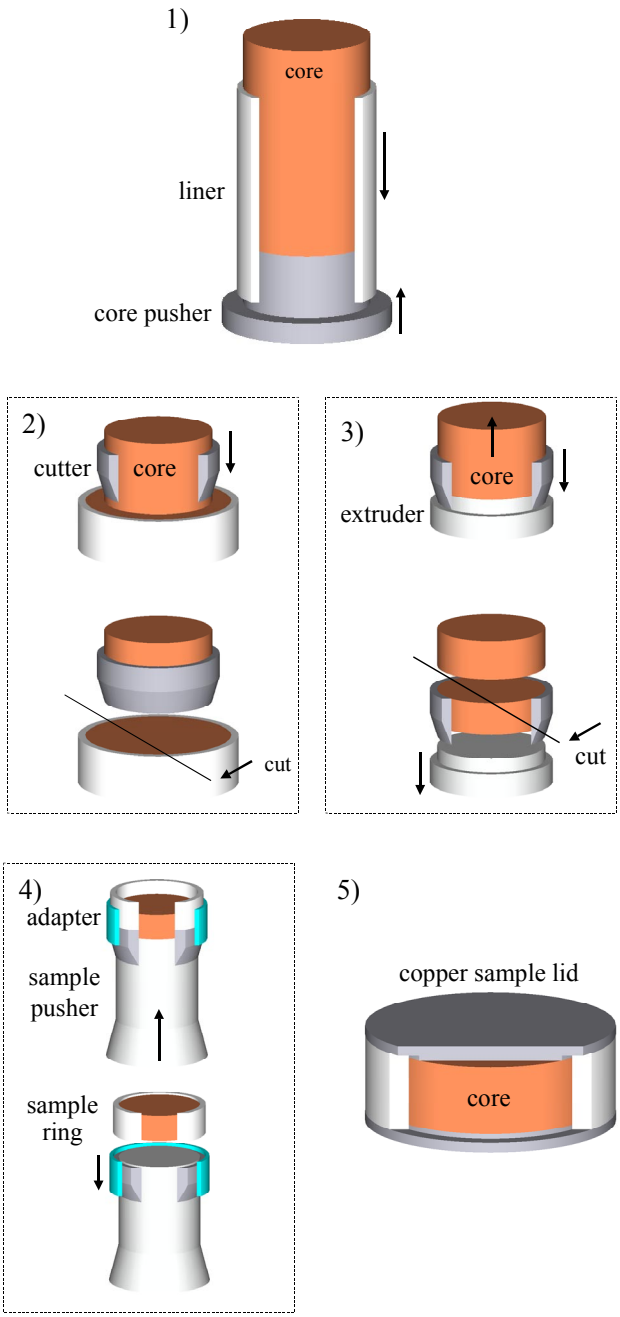

Figure A3. Sampling Leg 168 cores for divided-bar measurements. 1) The sediment core is pushed out of the core liner. 2) A cylinder with the diameter of the divided-bar stack is cut out of the soft sediment. 3) The core sample is pushed out of the core cutter and shortened to the desired thickness. 4) The core sample in the cutter is pushed into the plexiglas sample ring. 5) Two copper lids are placed on the top and the bottom of the sample ring. The resulting disk has an outer diameter of 50 mm and a height of 20 mm. The sediment sample inside has a diameter of 46 mm and a height of 14 mm. Measured in the divided-bar, this sample will provide the vertical component of thermal conductivity. To obtain the horizontal component, step 2) is performed perpendicular to the core liner axis.

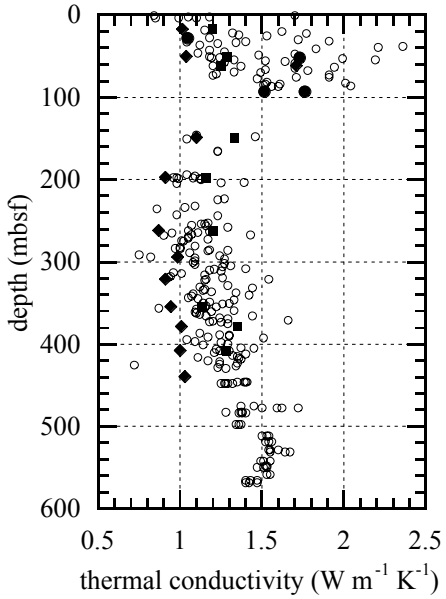

Figure A4. Comparison of thermal conductivity measured at laboratory temperature from shipboard line-source (open circles) and divided-bar measurements (for mud: vertical (diamonds) and horizontal (squares) components; for sand: solid circles).

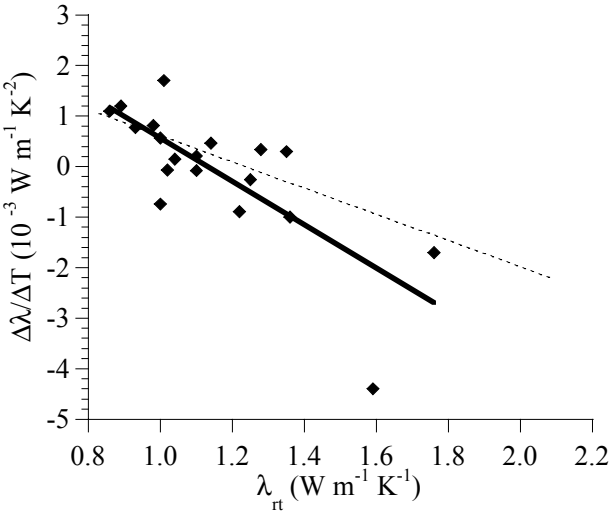

Figure A5. Temperature dependence $\Delta\lambda/\Delta T$ as a function of thermal conductivity at 20ºC (λ_{rt}). Solid symbols and solid line: this study; the two largest λ_{rt}–values are from sand samples; dashed line: theoretical dependence based on the geometric mixing model, temperature dependence of water and acid rocks, and porosity ranging from 0.2 to 0.8.

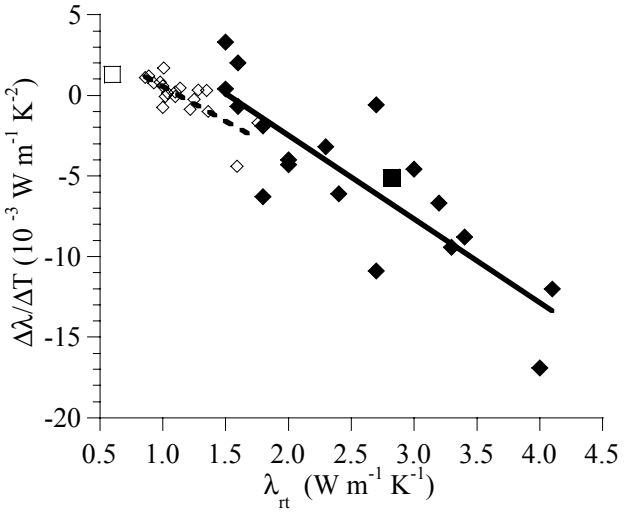

Figure A6. Temperature dependence $\Delta\lambda/\Delta T$ as a function of thermal conductivity at 20ºC (λ_{rt}) for bulk (open symbols) and matrix (solid symbols) thermal conductivity. The open square represents the value for seawater, the solid square for matrix.

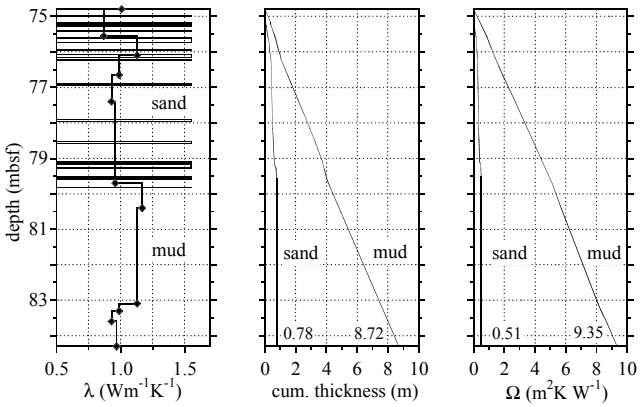

Figure A7. Example for the calculation of thermal resistance with equation (A15) for a layer between two temperature measurements at 74.8 mbsf and 84.3 mbsf (upper and lower boundary of figures) in Hole 1023A. Left: thermal conductivity from shipboard measurements of mud samples, corrected for anisotropy and temperature (solid symbols). Thin horizontal bars indicate position of sandy layers (from core description); the temperature corrected sand conductivity is shown by the endpoints. Center: cumulative thickness of sand and mud layers ($d_{S,j}$=0.78 m and $d_{M,j}$=8.72 m, respectively). Right: cumulative thermal resistance for mud, using single measurements and equation (A13): $\Omega_{M,j}$=9.35 m^2W/K; cumulative thermal resistance for sand, using the cumulative thickness ($d_{S,j}$) and the average conductivity of bars on the left ($\lambda_{S,j}$): $\Omega_{S,j}=d_{S,j}/\lambda_{S,j}$=0.51 m^2W/K. The thermal resistance for this layer (j=7) is the sum of both thermal resistances weighted with the relative thickness of sand and mud: Ω_7=0.78/9.5 * $\Omega_{S,7}$ + 8.72/9.5 * $\Omega_{M,7}$ = 8.62 m^2W/K.